



# JGR Atmospheres

## RESEARCH ARTICLE

10.1029/2019JD030928

### Key Points:

- The first laboratory study comparing spume generation in freshwater and real seawater under hurricane-force wind speeds has been conducted
- Across all particle sizes and wind speeds tested, significantly more seawater spume was produced than in freshwater conditions
- As compared to freshwater, the distribution of seawater spume particles in the air was significantly more concentrated near the water surface

### Correspondence to:

S. Mehta,  
sanchit.mehta@rsmas.miami.edu

### Citation:

Mehta, S., Ortiz-Suslow, D. G., Smith, A. W., & Haus, B. K. (2019). A laboratory investigation of spume generation in high winds for fresh and seawater. *Journal of Geophysical Research: Atmospheres*, 124, 11,297–11,312. <https://doi.org/10.1029/2019JD030928>

Received 2 MAY 2019

Accepted 14 OCT 2019

Accepted article online 23 OCT 2019

Published online 14 NOV 2019

## A Laboratory Investigation of Spume Generation in High Winds for Fresh and Seawater

S. Mehta<sup>1</sup> , D. G. Ortiz-Suslow<sup>2</sup> , A. W. Smith<sup>1</sup>, and B. K. Haus<sup>1</sup> 

<sup>1</sup>Department of Ocean Sciences, University of Miami, Miami, FL, USA, <sup>2</sup>Department of Meteorology, Naval Postgraduate School, Monterey, CA, USA

**Abstract** Given spume's role in mediating air-sea exchange at the base of tropical cyclones or other storm events, the focus of studies on spray dynamics has been within the marine environment. In contrast, spume production in nonseawater bodies has been underexplored and potential differences between sea and freshwater are neglected. The laboratory remains the primary means for directly observing spray processes near the surface because of the challenges to making robust field measurements. There is no standardization on the water type used for these experiments, and the effect this has on the generation process is unknown. This adds uncertainty in our ability to make physically realistic spume generation functions that are ultimately applied to the geophysical domain. We have conducted a laboratory experiment that aims to address this simple, yet overlooked, question of whether water type impacts the spume droplet concentration entrained in the air flow above actively breaking waves. We compared directly imaged concentrations for fresh and seawater droplets produced in 10-m equivalent winds from 36–54 m/s. Substantially higher concentrations of seawater spume were observed, as compared to freshwater across all particle sizes and wind speeds. The seawater particles' vertical distribution was concentrated near the surface, whereas the freshwater droplets were more uniformly distributed. Our statistical analysis of these findings suggests significant differences in the size- and height-dependent distributions response to increased wind forcing between fresh and seawater. These unexpected findings suggest an unanticipated role of the source water physiochemical properties on the spume generation mechanism.

## 1. Introduction

### 1.1. Motivation

Sea spray liquid droplets are ejected from the sea surface generally due to breaking waves and other related phenomena, such as bubble bursting in whitecaps. Once separated from the surface, and depending on their size, these droplets may reside within the marine atmospheric boundary layer (MABL) from fractions of a second to weeks. Once entrained in the MABL, they can interact with the ambient environment and mediate the air-sea fluxes of sensible and latent heat over a wide range of spatial and temporal scales (Andreas, 1992). This process is highly complex and remains a significant challenge to both observations and model within the geophysical domain.

In general, spray droplets are known to form via two main mechanisms: bubble bursting and spume generation. In the first mechanism, wave breaking causes air to be entrained in the water, which creates bubbles that rise to the surface, forming whitecaps (Monahan, 1972). Blanchard (1988) showed that a single bubble bursting event is a very energetic phenomenon that creates drops of two distinct types: film and jet drops. Film drops are generated when the bubble bursts and the surface film shatters; the receding rims become unstable and may eject anywhere from several to a few hundred droplets with radii ranging from 0.01 μm to a few micrometers (Spiel, 1998). Jet droplets are the second category of bubble-generated sea spray and are formed when a single bubble cavity collapses, thus forming a central “jet” that becomes unstable and breaks apart into anywhere from one to six individual particles (MacIntyre, 1972; Resch & Afeti, 1991; Spiel, 1997). This column of water, or Rayleigh jet, results from the rebound, or overshoot, of the sea surface caused by its own surface tension. Jet droplets typically dominate the spray droplet flux spectrum in the 3- to 20-μm radius range.

The bubble generation process is indirectly related to the tangential wind stress and individual wave breaking, whereas spume droplets are an example of particles directly produced from these mechanical processes (Monahan et al., 1986). On formation, spume droplets typically have radii larger than 25 μm. The wind speed

threshold for spume generation is approximately 7–11 m/s (Monahan et al., 1983). While it has been most common to parameterize spume generation via wind speed and fundamental droplet microphysics (e.g., Fairall et al., 1994), it is intuitively expected that the generation of this class of sea spray will be physically dependent on a host of processes converging on the air-sea interface in moderate to very high wind conditions (Fairall et al., 2009; Mueller & Veron 2009; Andreas et al., 2015).

Spume droplets comprise the larger regime of spray particles and have radii typically between 25  $\mu\text{m}$  and several millimeters. These droplets are generally assumed to be produced by the mechanical disruption of wave crests by the tangential wind stress and because of this very large spray volumes are expected in very high wind speed conditions (e.g., storms and tropical cyclones). These spume droplets have been shown to significantly mediate the interfacial fluxes of heat, moisture (Andreas 1992), and momentum (Andreas, 2004) across the air-sea interface. In the laboratory, Jeong et al. (2012) demonstrated that the unmeasured spray-mediated fluxes may account for up to a 38% increase in the overall moist enthalpy transfer coefficients at high winds. However, large uncertainties remain in our understanding of the spume generation and distribution within the MABL, particularly very near the actively breaking surface, simply due to the challenges of making accurate measurements in such extreme conditions.

Over recent decades, several investigators have proposed various explanations for the direct mechanism that forms spume. While it was generally known that wave breaking was related to spume, the direct physical mechanism was only recently theorized and/or described in the literature. Soloviev et al. (2017) showed, through their numerical experiments, that microscale wave breaking caused the disruption of the air-sea interface due to the presence of Kelvin-Helmholtz instabilities. At high winds, this results in the intense formation of foam at the surface and spume droplets entrained in the air. The laboratory experiments conducted by Troitskaya et al. (2018) provided the first physical evidence for several phenomena responsible for the direct generation of spume droplets at or near the wave crest. In summary, they found that bag breakup was the dominant mechanism for spume droplet generation at high winds. During a bag breakup event, an increase in the small-scale elevation of the water surface results in the formation of a kind of hydrodynamic sail, which “inflates” into a canopy bordered by a thicker rim; this sail eventually ruptures thus producing spume drops.

Several field and laboratory studies have shown that the aerodynamic drag coefficient tends to saturate as the 10-m, neutral wind speed approaches 30 to 40 m/s (Donelan et al., 2004; Potter et al., 2015; Powell et al., 2003). This regime coincides with the initiation of intense wave breaking and significant spume generation, which leads to the development of a distinct spray layer within the atmospheric surface layer, the atmospheric domain closest to the surface. The spray acts as an important thermodynamic layer that can mediate the balance between moist enthalpy input and wind energy dissipation at the air-sea interface (Haus et al., 2010). Accounting for spray-mediated fluxes has been shown to be an important factor in tropical cyclone modeling as it is considered a crucial in the development of hurricanes and severe extratropical storms. These spray droplets are responsible for the enhancement of energy flux from the ocean to the atmosphere as demonstrated in numerous modeling and experimental studies so far (Andreas, 2011; Andreas & Emanuel, 2001; Bao et al., 2011; Bianco et al., 2011; Soloviev et al., 2014; Takagaki et al., 2012). These processes have been the focus of much investigation in the marine environment (Andreas et al., 2015; Monahan et al., 2017).

Recent studies (Balaguru et al., 2012; Rudzin et al., 2019) have shown that the enthalpy flux at the base of tropical cyclones is impacted when these storms travel over salinity-induced barriers like river plumes. These studies suggest that accounting for the salinity of the water types is an important factor in accurately predicting the energy flux to/from the storm.

## 1.2. Spray Generation Dependence on Water Properties

Spray generation by bubble bursting is driven by the dynamics of the subsurface bubble plume and is highly sensitive to the differing physiochemical properties (like surface tension, viscosity, and density) of the underlying water mass (Monahan, 1967; Monahan & Zietlow, 1969). For example, various studies have shown significant differences in the size distribution and number of bubbles produced in laboratory simulations of breaking waves within fresh versus seawater. For bubbles with radii up to 100  $\mu\text{m}$ , Haines and Johnson (1995) found significant differences for individual bubbles when comparing fresh to seawater. They used a photographic method to investigate the size spectrum of bubbles in the plume generated by falling water

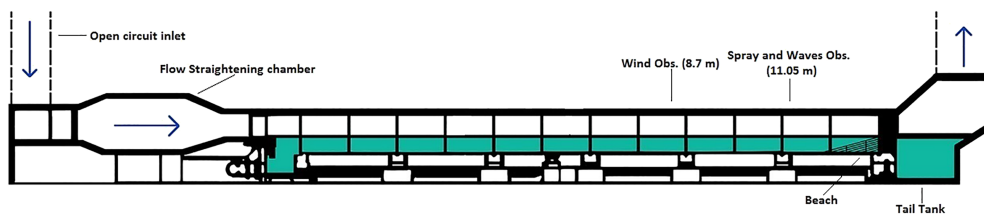


**Figure 1.** A schematic of the Air-Sea Interaction Saltwater Tank facility setup for this study. Color visualizes the water level, 0.42 m.

—to simulate a breaking wave. Bubbles were more numerous, smaller, and resided longer in the seawater plume than in freshwater. Later, laboratory experiments by Slauenwhite and Johnson (1999), found that 4–5 times more bubbles were produced in seawater as opposed to freshwater.

As compared to the bubble formation process, the role of varying water type in spume generation is not well established. Regardless, for the purposes modeling spume generation, it is assumed that this process is primarily mechanical and that physiochemical effects are secondary or negligible. Fairall et al. (2009) attempted to use laboratory experiments to compare spume ( $r_0 = 15\text{--}600 \mu\text{m}$ ) volume spectra in fresh and salted water (up to 24 practical salinity unit, PSU). While they found little difference between these water types, a comprehensive, quantitative analysis was lacking. Some limitations to this work included the use of a cloud imaging probe, which is limited in its ability to resolve larger droplets, the use of simulated seawater at a much lower salinity than found in the ocean, and the combined used of wind and mechanical waves. For these reasons, there are still unanswered questions and gaps in our understanding of the role salinity plays in spume generation. As far as the authors are aware, there have not been any attempts to directly address this question experimentally.

To test directly test the hypothesis that there is no difference between spume production in fresh versus sea water, a laboratory experiment was conducted comparing the observed, size-dependent distribution of spume entrained in a controlled air volume above fresh and seawater under hurricane-force wind conditions. This represents one of, if not the only, quantitative assessments of the varying rates of spume generation between the two water types using real seawater. The findings of this work directly test the general assumption that spume generation is controlled primarily by the mechanical wave-breaking process. This holds significant implications, not only for the theoretical or laboratory-based study of spume generation but also for the distinct role of spume generation in fresh versus seawater.

## 2. Methods

A brief summary of the experimental design and analytical methodology with specific details relevant to this study has been described in this section. Further relevant details can be found in Ortiz-Suslow et al. (2016), which focused only on the seawater data. The reader is directed to this previous work for more details.

### 2.1. The Facility

The experiment was conducted in the University of Miami's Air-Sea Interaction Saltwater Tank (ASIST), which is an acrylic wind-wave-current flume with a cross section of  $1 \times 1 \text{ m}$  and length 15 m (Figure 1). The mean water level was set to 0.42 m. In this study, wind was the primary forcing on the system. This experiment did not assess the impact of mechanically generated waves on spume generation.

### 2.2. Water Characteristics

The seawater used here was sourced from a nearby tidal inlet (Bear Cut) with a salinity of ~34 PSU, which is fully exposed to Atlantic Ocean water with no nearby freshwater sources. The seawater was pumped into the facility and stored in a reserve tank on top of the building. This allowed suspended particulates to settle out before being pumped through a sand filter and then a  $10\text{-}\mu\text{m}$  cartridge filter before pumping into ASIST. The freshwater source was the local municipal water system.

**Table 1**  
Summary of the In-Tank, Mean Conditions and Image Processing Evaluation

Level	$U_{10}$	$u_*$	$H_s$	Seawater	Freshwater
Lower panel	36	1.7	29	60% (7)	61% (7)
	40.5	2.0	32	75% (7)	78% (7)
	45	2.2	35	80% (7)	67% (7)
	49.5	2.4	36	82% (7)	84% (7)
	54	2.7	38	92% (7)	91% (7)
Middle panel	36	1.7	29	62% (7)	63% (7)
	40.5	2.0	32	80% (9)	80% (7)
	45	2.2	35	85% (7)	76% (7)
	49.5	2.4	36	85% (9)	84% (7)
	54	2.7	38	78% (8)	80% (7)
Upper panel	36	1.7	29	—	61% (7)
	40.5	2.0	32	—	79% (7)
	45	2.2	35	—	67% (7)
	49.5	2.4	36	—	83% (7)
	54	2.7	38	—	87% (7)

Note. The 10-m equivalent wind speed ( $U_{10}$ ) and friction velocity ( $u_*$ ), in meters per second, are given, along with the significant wave height ( $H_s$ ) in millimeters. The two rightmost columns give the visually verified percent success rate of the automatic droplet identification and the number of runs. The lower, middle, and upper panels refer to the three image frame heights used to reconstruct the profiles. This table is adapted from Ortiz-Suslow et al. (2016).

### 2.3. Instrument Locations

Spray observations were made 11.05 m downwind of the air inlet. Wind was measured at an elevation of 29 cm above mean water level by a three-dimensional sonic anemometer positioned 6.60 m downwind of the inlet. Maximum 10-m equivalent wind speed was calculated to be 54 m/s. This 10-m referencing was done following earlier ASIST work presented by Haus et al. (2010) and Donelan et al. (2004). The wave heights (Table 1) in the tank were measured at the location of the spray observations using a downward looking ultrasonic distance meter sampling at 10 Hz.

### 2.4. Camera Setup

Spume droplets were imaged using a Dantec Dynamics particle image velocimetry acquisition system modified to be used in a shadow imaging mode. A camera was positioned outside of the tank and oriented to be looking into a high intensity strobe, also mounted outside of the tank, but directly opposite the camera. A wiper was placed on the inside of the tank's acrylic wall, facing toward the camera to minimize the accumulation of droplets on the acrylic. The image acquisition timing and strobe pulse were controlled and synchronized using the Dantec system. As spray was ejected into the air volume in the tank, the droplets would appear as shadows (or silhouettes) in the camera images. The geometry of the setup was such that the camera imaged a 55-mm × 75-mm plane in the middle of

the tank aligned with the along-tank direction. A total of five wind trials was conducted in the tank, with  $U_{10}$  ranging from 36 to 54 m/s (Table 1).

For each  $U_{10}$  and water type, the camera-strobe system was setup at two vertical levels relative to the water surface (an additional height was done for freshwater). These levels, labeled Lower, Middle, and Upper panels in Table 1, were centered on different heights above the still water level and arranged such that they created a continuous virtual stack. The imagery from each independent level was stitched together to create the spume droplet concentration profiles extending over the scaled height, from  $z/H_s \sim 2$  to 6. Here,  $z$  is the height above the mean water level in the tank, and  $H_s$  is the significant wave height for a particular wind speed (determined using zeroth moment of the elevation variance spectrum). Using the geometry of the setup, any overlap between panels was removed prior to analyzing the spume droplet distributions.

### 2.5. Data Collection Protocol

For each level, the wind was allowed to ramp up and time (120 s) was allowed for the tank conditions to become stationary. Then at least seven consecutive sets of 250 images were acquired, 250 being the computational memory limit. Unfortunately, the ambient water temperature in the tank was not recorded. However, the laboratory was climate controlled and, before using a freshly pumped volume of water, the tank was allowed to acclimatize to room temperature (~23 °C). A typical set of 7 × 250 image acquisitions took approximately 10 min to complete, and after each trial the water level was returned to 0.42 m (water loss was due to spray advecting into air outlet).

### 2.6. Image Calibration and Processing

The image processing was independently carried out on each set of 250 images. In total, over 52,000 images were acquired and processed for this experiment. The Dantec shadow imaging software tool was used to contour the in-focus droplets in the image and determine their centroid location in the frame as well as their two-dimensional projected surface area. A preexperiment calibration was done to determine that the image resolution was 42  $\mu\text{m}/\text{pixel}$ . The droplet contouring found the two-dimensional projected surface area of each droplet. Assuming spherical drops, the equivalent radius of observed drops ranged from 80 to just over 1,400  $\mu\text{m}$ . The smallest drop that could be measured using this method encompassed a two-dimensional area of ~16 square pixels (which equals 28,224  $\mu\text{m}^2$ ).

## 2.7. Spray Droplet Identification and Sizing

The efficacy of the automatic droplet contouring was tested against visual inspection of every 25th image of each 250 image set. The success of the processor was defined as the number of properly identified, in-focus droplets over the number of droplets identified via inspection (see Table 1). In general, the processor tended to undercount the total number of droplets per image, and there was not a significant difference in the success rate between fresh and seawater. The images from the 45-m/s trial in freshwater conditions were found to be substantially more difficult for the processor to automatically count. In the postexperiment data quality control and assessment, this was visually determined to be due to poor image contrast for this particular trial (wind speed + water type). After taking additional steps to increase the contrast, the results of the visually checked processing results (Table 1) remained anomalously low as compared to all the other data sets. As a result, this wind speed (for both water types) was removed from the comparative analysis. Simply repeating these experiments was not an option because in the interim between concluding the experiments (ca. 2013) and conducting the analysis where this problem was discovered (ca. 2015), the ASIST had been moved to a new facility and reconfigured in such a way as to preclude repeating these experiments in exactly the same manner.

The radius- and vertical height-dependent droplet concentration profiles were determined by discretizing the identified droplet distributions into 50- $\mu\text{m}$ -wide radius classes and 3-mm vertical cells. Therefore, the number concentration for each radius bin and vertical cell at a given wind speed becomes

$$n(r_i, z_j) = \frac{\text{Count}(r_i, z_j)}{\Delta \text{Vol} N_{\text{total}} dr} \quad (1)$$

where  $\text{Count}(r_i, z_j)$  is the total number of observed droplets in the  $i$ th radius class and  $j$ th vertical cell,  $\Delta \text{Vol}$  is the air volume of each vertical cell,  $N_{\text{total}}$  is the total number of images in an observation period (e.g.,  $7 \times 250 = 1,750$  images), and  $dr$  is the width of each radius class (50  $\mu\text{m}$ ). From this, the vertically integrated mass concentration was obtained by multiplying the corresponding water density,  $\rho$ , for the two media, to the volume concentration at each radius class as

$$m(r_i) = \frac{4}{3} \pi \rho \int r_i^3 n(r_i, z) dz \quad (2)$$

## 3. Results

The results presented here are based on spume droplet observations collected using a nonobtrusive, optical method quantifying the droplet distribution in the air mass directly above the water surface, for 10-m equivalent winds from 36 to 54 m/s in both fresh and seawater (herein, FW and SW, respectively). These will be discussed here as overall spume droplet number concentrations  $n(r, z)$ , vertically integrated number concentration,  $n(r)$ , and radius-integrated number concentration,  $n(z)$ . In addition, a statistical analysis of  $n(r)$  and  $n(z)$  is presented to provide a quantitative comparison between the radius- and height-dependent distributions for FW and SW, respectively.

### 3.1. Overall Number Concentration, $n(r, z)$

A two-dimensional representation of the variability in the overall spume droplet number concentration,  $n(r, z)$  for FW and SW is shown in Figure 2. For both FW and SW across all droplet sizes,  $n(r, z)$  decreased with height above the interface and increased with  $U_{10}$ . However, there were differences between the two water types.

With the  $U_{10}$  increasing from 36 to 54 m/s,  $n(r, z)$  increases more for the SW than FW. This can be seen in the corresponding SW and FW panels in Figure 2. For example, in FW, the percentage of filled grid space that was observed increased from 16% to 62%, whereas for SW, the grid space increased from 17% to 76% between the lowest and highest measured  $U_{10}$ , respectively. While not a generalizable metric, this filling of the grid space represents the fraction of the imaged air volume where additional spray was observed for each increase in  $U_{10}$ . The distribution of droplet number concentration was found to be skewed toward the smaller radii for both water types, indicating the dominance of smaller radii droplets in terms of pure quantity. This is

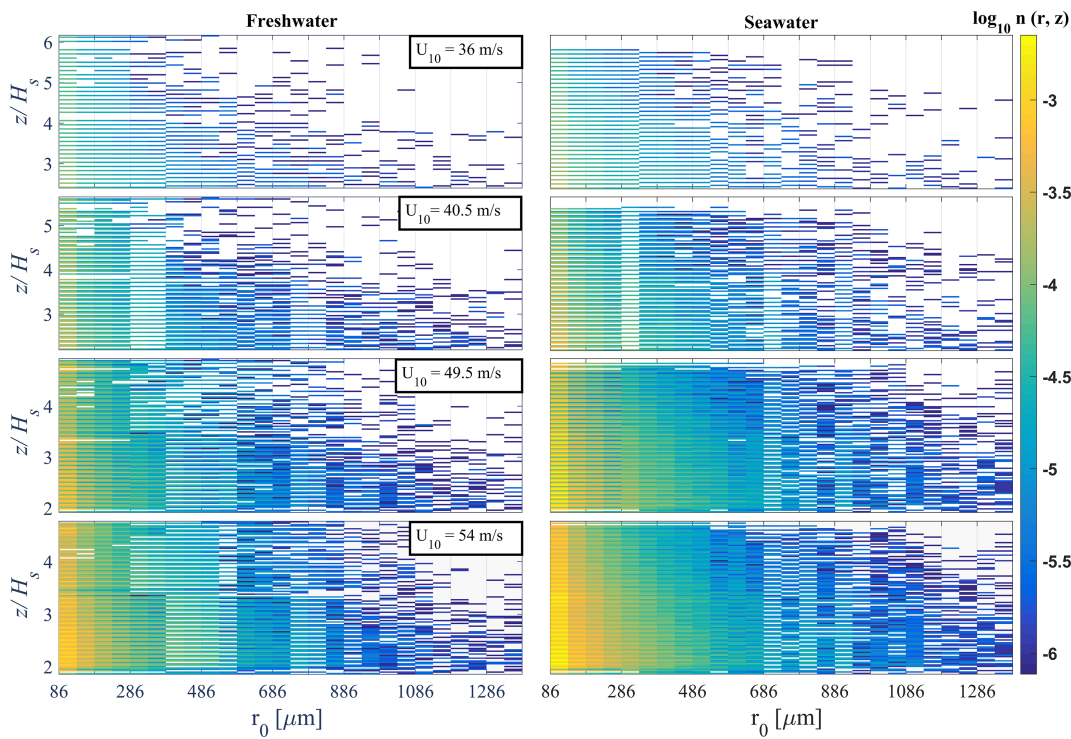


**Figure 2.** Two-dimensional distribution of overall observed spume droplet number concentration as a function of observed scaled height and binned droplet radius for freshwater (left column) and seawater (right column) are shown at different wind speeds from top to bottom. The color bar is common across all panels. Gray cells represent no droplets counted.

intuitive, since the largest droplets would be expected to be more rarely imaged due to their low residence time in the air flow and resistance to vertical diffusion (Andreas et al., 2010).

The total spume droplet number concentration  $n_{\text{total}}$  (double integration of  $n(r, z)$ ) increased as  $U_{10}$  increased. From the lowest to highest  $U_{10}$ ,  $n_{\text{total}}$  increased by 30 and 25 times for SW and FW, respectively. Relative to  $n_{\text{total}}(\text{FW})$ ,  $n_{\text{total}}(\text{SW})$  was greater by a factor varying from 1.5 to 2.5, depending on the  $U_{10}$  (Table 2).

### 3.2. Vertically Integrated Number Concentration, $n(r)$

The variability in the vertically integrated number concentration  $n(r)$ , (Figure 3a) and mass concentration,  $m(r)$ , (Figure 3b) are shown as a function of the spume droplet radius for different  $U_{10}$ .

Overall,  $n(r)$  values for both water types steadily increased as  $U_{10}$  increased and decreased as droplet radius increased. The size dependence of  $m(r)$  was more complex and nonlinear as compared to the number concentration (Figure 3b). The ratio  $n_{\text{SW}}/n_{\text{FW}}$  was generally  $>1$  for all radius classes except five instances ( $r_0 = 686 \mu\text{m}$  at  $U_{10} = 54$  m/s;  $r_0 = 936\text{--}986 \mu\text{m}$ ,  $1,236\text{--}1,286 \mu\text{m}$  at  $U_{10} = 36$  m/s), which comprise ~5% of the observations (Figure 3c).  $n_{\text{SW}}/n_{\text{FW}}$  was only ever  $<1$  for 36 m/s, except for one radius class at 54 m/s. Apart from this,  $n_{\text{(SW)}}/n_{\text{(FW)}}$  ranged from 1 to 4.6. While  $n_{\text{SW}}/n_{\text{FW}}$  varied with radius, for all but two classes,

this ratio increased with wind speed up to 49.5 m/s, and only a few classes exhibited this trend monotonically. Interestingly, there was a substantial drop in  $n_{\text{SW}}/n_{\text{FW}}$  between 49.5 and 54 m/s for the lower half of the radius spectrum. This became less consistent when  $r_0 > 900 \mu\text{m}$ . In general, the differences between SW and FW increased with wind speed.

For a given wind speed,  $m(r)$  increased rapidly with increasing particle radius, but at about 400  $\mu\text{m}$ , all  $m(r)$  exhibited a leveling off, followed by a decrease in  $m(r)$  with increasing radius above 900  $\mu\text{m}$ , which was most pronounced for the highest wind speeds. In order to explore this behavior more fully,  $m(r)$  was segregated into three radius subranges (Figure 4)

**Table 2**  
Summary of  $n_{\text{total}}(\text{SW})$  and  $n_{\text{total}}(\text{FW})$  for All Wind Speeds

$U_{10}$	$n_{\text{total}}(\text{SW})$	$n_{\text{total}}(\text{FW})$	$\Delta = n_{\text{total}}(\text{SW} - \text{FW})$	$R_{sf} = n_{\text{total}}(\text{SW})/n_{\text{total}}(\text{FW})$
36	6,100	4,100	2,000	1.5
40.5	25,400	16,200	9,200	1.6
49.5	126,500	51,400	75,100	2.5
54	183,900	102,700	81,200	1.8

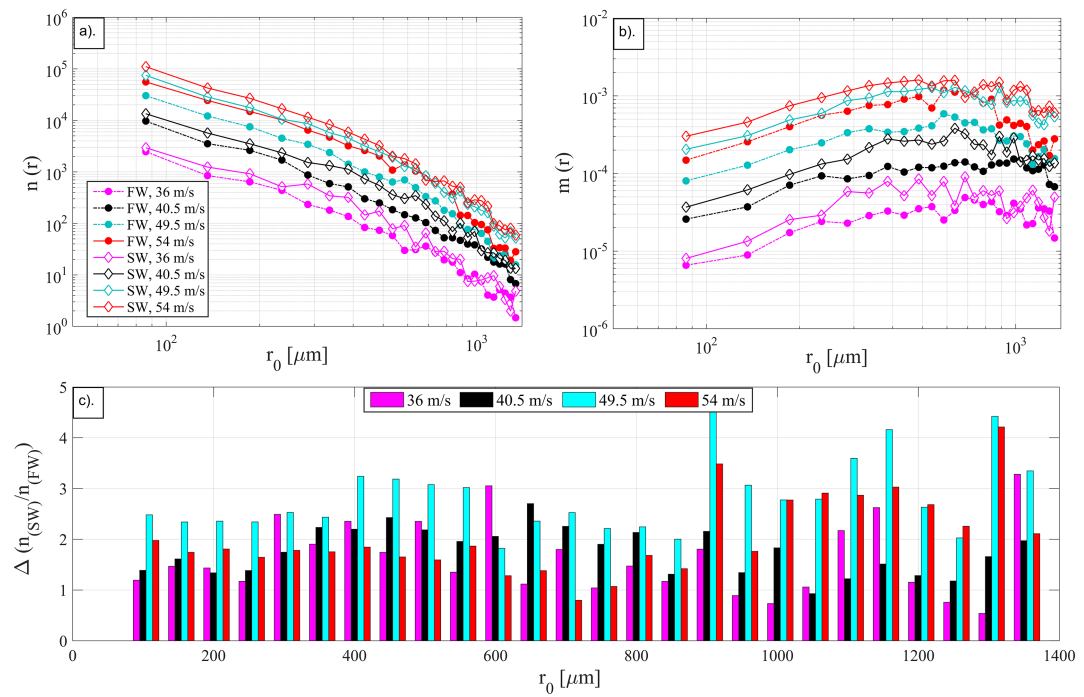


**Figure 3.** Vertically integrated number concentration (number per cubic meter per micrometer) spectra (a), vertically integrated mass concentration ( $\text{kg/m}^3/\mu\text{m}$ ) spectra (b), and the distributions of  $n_{SW}/n_{FW}$  (c), all plotted against the observed droplet radius,  $r_0$  and for each wind speed.  $r_0$  is referenced to the first discrete radius within each 50- $\mu\text{m}$ -wide class.

based on our qualitative assessment of the spectra. In the first droplet size subrange ( $r_0 = 86\text{--}400 \mu\text{m}$ ), both  $m(r)_{SW}$  and  $m(r)_{FW}$  increased with radius and  $U_{10}$ . The mean increase in  $m(r)$  was a factor of 22 and 27 for FW and SW, respectively, as  $U_{10}$  increased from 36 to 54 m/s. For the lowest two wind speeds, the  $m(r)_{SW}$  increased more rapidly than  $m(r)_{FW}$  with  $r_0$ , suggesting that SW droplets were more readily generated as compared to FW for the same ambient wind speed. In the second subrange ( $r_0 = 400\text{--}900 \mu\text{m}$ ),  $m(r)$  tended to be independent of droplet radius (i.e., best fine line exhibited a negligible slope) for both water types. In the third subrange ( $r_0 = 900\text{--}1,400 \mu\text{m}$ ),  $m(r)$  for both water types decreased with the increasing

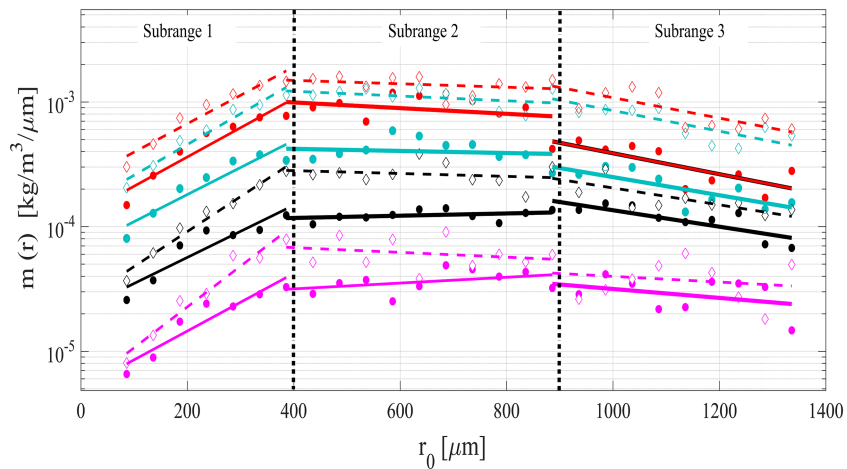


**Figure 4.** Freshwater (FW) and seawater (SW)  $m(r)$  from Figure 3b, segregated into three radius subranges: 1, 2, and 3 marked by vertical dashed lines. The solid and dashed lines represent the least squares linear relation between  $\log(m(r))$  and  $r_0$  for FW and SW, respectively. FW data have been shown in solid circles, and SW in diamonds with the corresponding  $U_{10}$  in meters per second (same as in Figure 3).

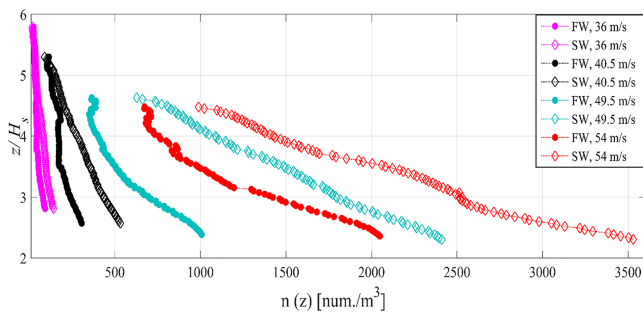


**Figure 5.** Vertical profiles of radius-integrated number concentration (in number per cubic meter) plotted against profiles scaled by the appropriate  $H_s$  for a given wind speed. FW = freshwater; SW = seawater.

calculations, the midbin radius class value was used to calculate the total mass in each sphere-equivalent spray volume.

### 3.3. Radius-Integrated Number Concentration, $n(z)$

Profiles of radius-integrated number concentration,  $n(z)$ , were analyzed to characterize the vertical distribution of FW and SW spume droplets (Figure 5). These profiles come directly from the two-dimensional number concentrations defined in equation (1) and Figure 2. Overall, across all  $U_{10}$ , more droplets were observed along each profile for SW rather than FW and the highest concentrations were observed near the surface, in both water types.

The majority of the differences in  $n(z)$  between FW and SW occurred closest to the surface. For the lowest two wind speeds,  $n(z)$  for these trials tended to converge at the top of the profile, whereas for 49.5- and 54 m/s trial, this convergence was not observed. Upon closer inspection of  $n(z)$ , for the highest two wind trials, it appears as if the two profiles are beginning to come together, but this was not fully resolved as to be definitive. This may have been a result of the fixed observation height  $z$  (relative to the mean water level) with a changing  $H_s$  as  $U_{10}$  increased. So the scaled region where convergence was observed ( $z/H_s > 5$ ) was not resolved at the higher winds.

### 3.4. Statistical Analysis of $n(r)$ and $n(z)$

Regression analysis was performed to derive empirical relationships for  $n(r)$  and  $n(z)$ , which are presented in Figures 3a and 5, respectively. For both of these analyses, the  $U_{10}$  dependence was also considered. This is an important exercise to formalizing the qualitative findings of these experiments as described above. These analyses build on a previous study conducted using just the SW data from these experiments (Ortiz-Suslow et al., 2016); furthermore, this statistical analysis provides a means of more directly and quantitatively comparing the findings from FW and SW.

The first empirical relation was functionally represented as

$$N_s = f(r_0, U_{10}) \quad (3a)$$

where  $N_s$  is the modeled vertically integrated droplet number concentration (i.e.,  $n(r)$ ) for both FW and SW (Figure 3a).  $n(r)$  were tested against three empirical relationships: a power law, an exponential, and a linear fit. The model that minimized the root-mean-square error (RMSE) between the observed  $n(r)$  and modeled  $N_s$  was chosen as best representing the observed values, for a given  $U_{10}$ . For both FW and SW, a power law performed best for all winds. The model correlation for the power law was very strong ( $R^2 \sim 0.99$ ,  $p$  values  $< 0.001$  for all fits) and substantially better than the two other relationships used in this test ( $R^2 \sim 0.85$  and  $\sim 0.93$  for the linear and exponential, respectively); furthermore, the RMSE for the power law was substantially higher than for the other model fits. Based on these results, we can define  $N_s$  as follows:

$$N_s = a r_0^b. \quad (3b)$$

Coefficients  $a$  and  $b$  are the empirically derived coefficients. Initially, this analysis was performed over the entire radius spectrum, but it was found that  $n(r)$  exhibits a nonlinear (in log-log space) transition in

droplet radius for all winds. The middle subrange appears to be a transition region between increasing and decreasing  $m(r)$  with increasing  $r_0$ . It is interesting to note that the peaks in these spectra are very broad, indicating that the majority of the water content entrained in the air is distributed over a wide bandwidth of droplet sizes.

In terms of aggregate spray loading, that is, the ratio of the total integrated mass concentration (over height and radius) divided by the atmospheric density, the observations capture an increase from approximately 1% to 17%, for SW, as wind speed increases from 36 to 54 m/s. The increase in spray loading for FW only reached  $\sim 10\%$ . These values, and rate of increase with wind speed, are comparable to numerical simulations showing the significant effect particles have on the near-surface turbulence (e.g., Pan et al., 2019; Richter & Sullivan, 2013). For these

**Table 3**

Regression Coefficients for SW and FW to the Empirical Number Concentration Profile Given in Equation (3b)

$r_0 < 500 \mu\text{m}$				$r_0 > 500 \mu\text{m}$			
$U_{10}$	$a$	$-b$		$a$	$-b$		$SW$
		$FW$	$SW$		$FW$	$SW$	
36	8.9E+00 (0.9E+06)	3.7E+06 (0.7E+06)	1.94 (0.17)	1.60 (0.21)	1.3E+10 (0.5E+10)	5.6E+10 (0.4E+10)	3.05 (0.44)
40.5	4.9E+07 (0.2E+07)	3.5E+07 (0.3E+07)	1.92 (0.25)	1.76 (0.08)	1.9E+10 (0.4E+10)	3.6E+12 (0.3E+12)	2.93 (0.30)
49.5	1.4E+08 (0.7E+08)	3.3E+08 (0.1E+08)	1.90 (0.10)	1.89 (0.07)	2.3E+15 (0.5E+15)	4.0E+13 (0.3E+13)	4.52 (0.32)
54	1.5E+08 (0.5E+08)	4.8E+08 (0.6E+08)	1.79 (0.08)	1.88 (0.07)	2.3E+15 (0.2E+15)	3.7E+13 (0.4E+13)	4.42 (0.50)

Note. The number of samples included in the regressions for  $r_0 < 500$  ( $> 500$ )  $\mu\text{m}$  was 9 (17). The values indicated in the bracket below correspond to the  $\pm 95\%$  confidence interval bounds. FW = freshwater; SW = seawater.

spectral slope at radii around  $500 \mu\text{m}$ . To better resolve the variability in  $n(r)$ , we performed the regression over two subranges, for  $r_0 < 500 \mu\text{m}$  and for  $r_0 > 500 \mu\text{m}$ , deriving coefficients two sets of  $a$  and  $b$  for these subranges independently. The RMSE-based selection criteria described above was applied to the subrange regressions as well with the same results. The results of this analysis are provided in Table 3, and the regression results as compared to the observed  $n(r)$  for SW and FW are provided in Figure 6.

For the smaller radii subrange,  $b$  (i.e., the spectral slope) for FW and SW was between approximately  $-2$  and  $-1.5$  but exhibited contrasting dependence on  $U_{10}$ . For FW,  $b$  monotonically increased from  $-1.95$  to  $-1.79$ , whereas for SW,  $b$  decreased from  $-1.60$  to  $-1.89$  and the slopes for the two highest wind speeds (SW only) were effectively the same. Values of  $a$  for both FW and SW were of a similar order of magnitude for all  $U_{10}$  and increased with increasing  $U_{10}$ . For the two lowest wind speeds, value of  $a$  was higher in FW but at two highest winds it was higher in SW. For the larger radii ( $r_0 > 500 \mu\text{m}$ ), unlike in the smaller droplet subrange, the spectral slopes ( $b$ ) for both FW and SW were negatively dependent on  $U_{10}$  and the transition for the former was much more substantial ( $-3$  to  $-4.5$ ). In general, we found that there was a significant change in both  $a$  and  $b$  from the lowest to highest wind speeds, across both water types, and that within each water type, the differences in  $a$  and  $b$  become relatively small to negligible for 49.5 and 54 m/s.

The second empirical relationship for  $n(z)$  takes the functional form:

$$N_v = f(z/H_s, U_{10}), \quad (4a)$$

where  $N_v$  is the modeled radius-integrated number concentration. Using a similar technique as above, a logarithmic fit for SW and a second-order polynomial fit for FW was found to best represent  $n(z)$  in the two respective water types. These relationships can be expressed as follows:

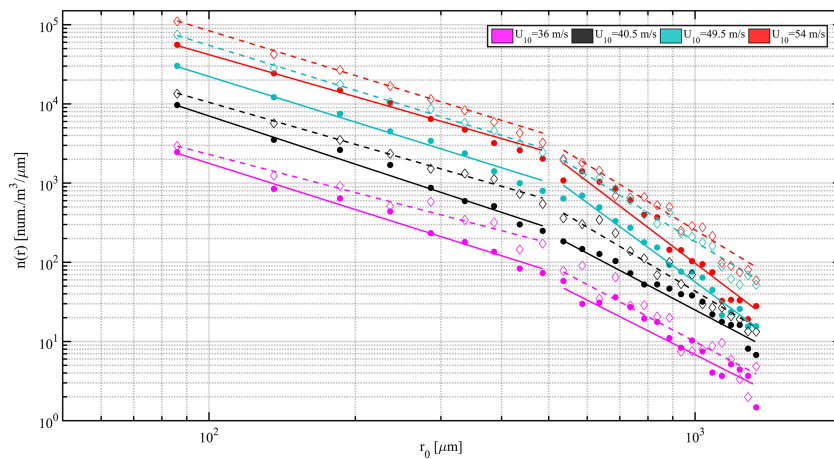


**Figure 6.** Results of performing least squares, log-scaled linear regression on the  $n(r)$  for seawater (solid dots) and freshwater (hollow diamonds) over the two radius subranges defined about  $500 \mu\text{m}$ , the coefficients of the regressions are provided in Table 3.

**Table 4**  
*Least Squares Regression Derived Coefficients From Equations (4b) (SW) and (4c) (FW)*

U <sub>10</sub> (m/s)	FW			SW	
	p <sub>1</sub>	-p <sub>2</sub>	p <sub>3</sub>	c	-d
36	4.0E-06 (0.6E-06)	1.2E-05 (0.3E-05)	3.1E-05 (0.6E-05)	4.21 (0.45)	0.21 (0.003)
40.5	9.0E-06 (1.4E-06)	3.8E-05 (0.8E-05)	1.3E-04 (0.4E-04)	3.85 (0.48)	0.21 (0.003)
49.5	6.5E-05 (1E-05)	1.8E-08 (0.5E-08)	4.0E-4 (0.5E-04)	3.37 (0.43)	0.20 (0.002)
54	1.2E-04 (0.3E-04)	4.0E-04 (0.8E-04)	8.6E-04 (1.2E-04)	3.26 (0.40)	0.20 (0.002)

*Note.* For each regression, the total sample size was 111 vertical cells. FW = freshwater; SW = seawater.

$$N_{v,sw} = \frac{\log(z/H_s) - \log(c)}{d} \quad (4b)$$

$$N_{v,fw} = p_1(z/H_s)^2 + p_2(z/H_s) + p_3, \quad (4c)$$

where  $N_v$  (sw) and  $N_v$  (fw) are the predicted radius-integrated droplet number concentration profiles for SW and FW, respectively. In order to confirm that two different functions are appropriate for FW and SW, respectively, the RMSE derived from applying both the logarithmic and polynomial expressions (4b) and (4c) to both FW and SW are given in Table 4. For all tests, the coefficients of determination were strong ( $R^2 \sim 0.96\text{--}0.99$ ), but there is a clear difference in the resulting RMSE. In general, the RMSE for the polynomial function applied to SW was at least 2–4 times larger than when applied to FW, and we found similar results when comparing the RMSE of a logarithmic function applied to FW versus SW. This provides a quantitative comparison to the clear, visually evident differences between  $N_v$  (sw) and  $N_v$  (fw) (see Figure 5). The coefficients for each empirical formula are given in Table 4.

## 4. Discussion

The aim of this study was to investigate whether water type impacts the generation of spume droplets, which has been generally assumed to be the result of the purely mechanical wave-breaking process. This relatively simple question was evaluated using a series of controlled experiments and the results of these tests indicate that there are substantial differences in the amount and vertical distribution of spume produced in FW and SW.

### 4.1. On the Analysis of the Radius- and Height-Integrated Number Concentration

The statistical analysis of  $n(r)$  revealed that there is a strong difference in the size-dependent concentration spectrum (for all wind speeds and both water types) for the smaller droplet ranges, relative to the larger drops. Hence, there is a clear difference in spectral slope for radii  $<500\text{ }\mu\text{m}$  versus  $>500\text{ }\mu\text{m}$ . It was interesting to note that the spectral dependence with wind speed varied across these subranges between FW and SW. While there are only four wind trials to compare, the robustness of the empirical analysis (i.e., fairly low uncertainty in  $a$  and  $b$ ) is encouraging to this reflecting a physical change in the rate of spume production and the characteristics of the size-dependent distribution of entrained spray above the breaking waves.

The analysis into  $n(z)$  provided mixed results, in empirical form, between FW and SW. For the latter, the radius-integrated concentration profiles (Figure 5) were very complex and applying a logarithmic profile, which worked well for SW, provided very poor results. Therefore, other functional forms were explored to simply identify the form that best represented the FW variance. While the second-order polynomial performed best (equation (4c)), the results were only slightly better (in terms of RMSE) than an exponential profile and for one trial, the latter model actually performed better. We would emphasize that this is purely an empirical exercise to describe these results, while there may be some physical implications of these findings, deriving the principle mechanism explaining a logarithmic versus quadratic concentration profile goes beyond the scope of this work—though the findings suggest it may be warranted.

Up to this point,  $n(z)$  and the statistical analysis has been concerned with the absolute concentration. However, the results of the  $n(r)$  analysis revealed that there is simply more spray produced in SW. To highlight the differences in the FW and SW vertical distribution while taking into account the absolute amount of

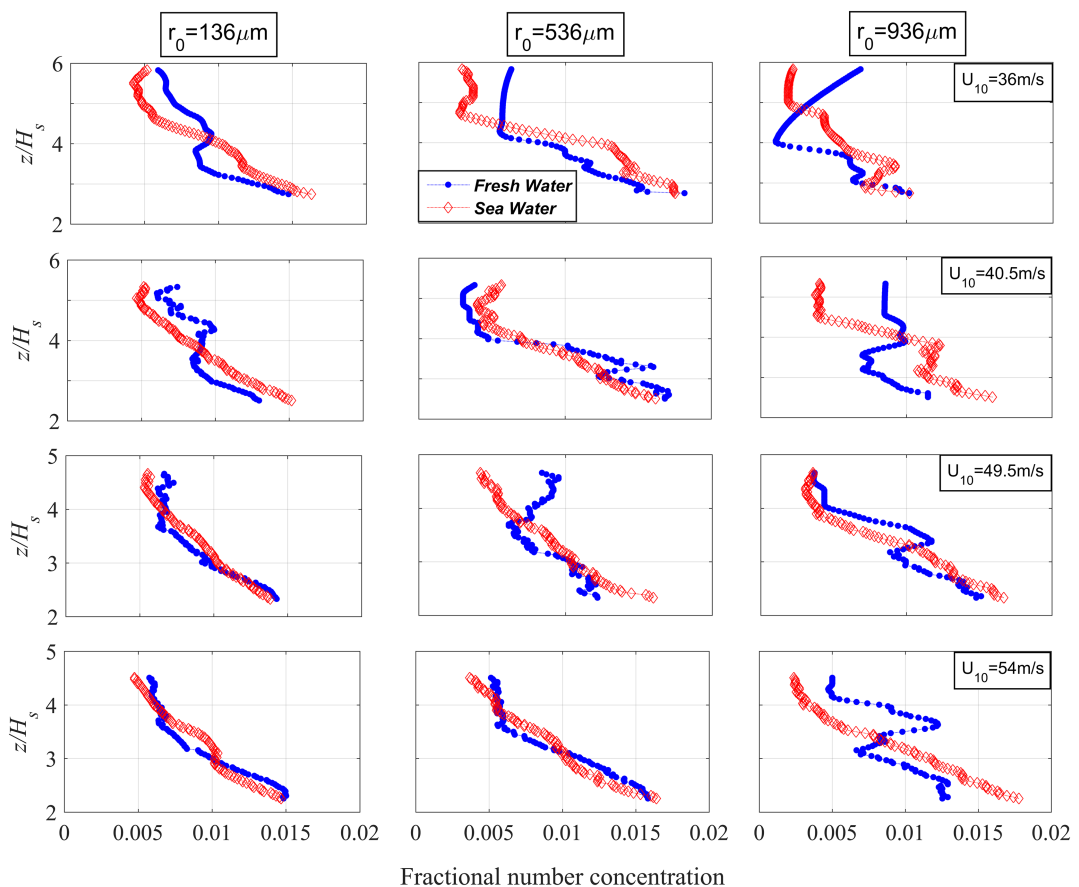


**Figure 7.** Selected profiles of spume droplet number concentration from Figure 2 at different wind speeds for freshwater and seawater. Each profile has been normalized by the total spume droplet number concentration value for that particular profile. The values at the top of each column mark the droplet radius class ( $\mu\text{m}$ ). X and Y axes are common to each plot and show the scaled height and fractional number concentration respectively. Freshwater and seawater data have been shown by red and blue dots, respectively.

spume produced, representative number concentration profiles from the subranges used in section 3.1 were normalized by their total, vertically integrated concentration (Figure 7). This essentially gives the fractional change in number concentration with scaled height  $z/H_s$ .

From this, we found that when compared to their corresponding FW profile, there were proportionally fewer SW droplets entrained in the air at the top of the profile. This was found for all but one of the profiles analyzed,  $r_0=536\mu\text{m}$  at  $40.5\text{ m/s}$ . This suggests that, while SW droplets are more readily produced for all radii and wind speeds than in FW, they are not as uniformly distributed in the vertical. Essentially, droplet production is more facilitated in SW, but the vertical transport of these droplets is somehow inhibited relative to FW.

#### 4.2. Comparison With Previous Experiments

A subset of the results from this study at  $U_{10}=36\text{ m/s}$  were compared with measurements presented by Fairall et al. (2009) for  $U_{10}\sim 32\text{ m/s}$  (Figure 8) and at  $U_{10}=40.5$  and  $49.5\text{ m/s}$  with the measurements reported by Veron et al., 2012; Figure 9). These comparisons are discussed here because the works of Fairall et al. (2009) and Veron et al. (2012) represent the only other available experiments in the literature with which to compare the results of this study.

Fairall et al. (2009) used FW and *salted* freshwater to compare the influence of different water types on spume production. Here, the FW and SW results of the present study were compared to the Fairall et al. (2009) FW and the salty water (SW\*, salinity of 24 PSU). Vertical profiles of particle number concentration

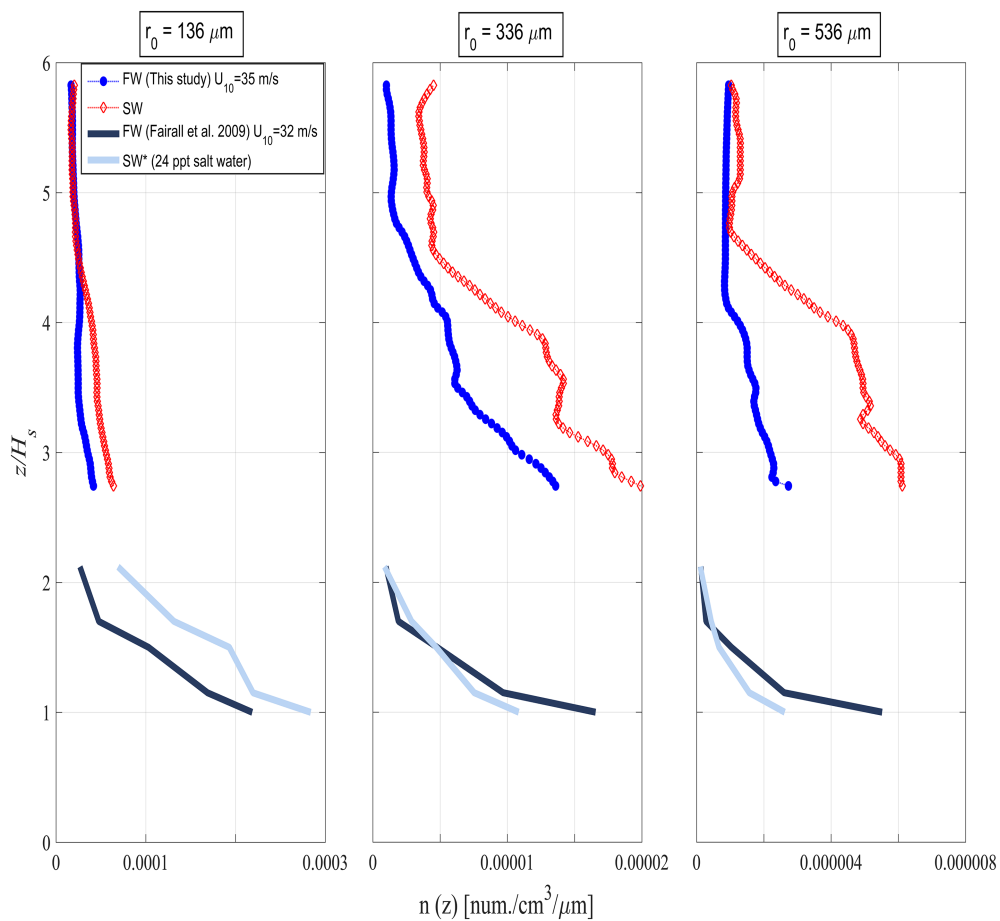


**Figure 8.** A comparison of vertical profiles for freshwater (FW) and seawater (SW) spume droplet number concentration (in number per cubic centimeter per micrometer) at three radius classes from a subset in this study (at  $U_{10} = 36$  m/s) and the observations reported in Fairall et al. (2009) at  $U_{10} = 32$  m/s. The legend bar is common to all three panels. FW and SW data from our study is in red and blue dots, respectively. Solid lines in brown and cyan show the fresh and saline water data from Fairall et al. (2009). The values at the top of each column mark the droplet radius ( $\mu\text{m}$ ).

at three different radius classes ( $r_0 = 136, 336$  and  $536 \mu\text{m}$ ) were constructed from the droplet volume size spectra defined as the volume of the droplets identified per unit sample air volume per unit radius increment ( $\text{cm}^3 \cdot \text{cm}^{-3} \cdot \mu\text{m}^{-1}$ ) in the original Fairall et al. (2009) article. The vertical gap observed in all the profiles in Figure 8 is a consequence of the differences in  $z/H_s$  observed in Fairall et al. (2009), which has a maximum  $z/H_s$  of 2.1, as compared to this study where the minimum  $z/H_s$  observed was 2.43.

In general, Fairall et al. (2009) measured lower number concentrations as well as less difference between fresh and saline water than was found in the present work. In addition, while the results of this study consistently demonstrate that less FW spume was produced near the water surface as compared to SW, the Fairall et al. (2009) results are mixed. The strongest agreement between these two studies occurred for the small particles with the profiles appearing to be consistent across the  $z/H_s$  gap.

Drawing specific, quantitative conclusions from the comparison with the Fairall et al. (2009) study is challenging, given the very different conditions in both experiments. In the Fairall et al. (2009), salt water was used as proxy for seawater along with the use of mechanical waves to simulate long period swell underneath a wind-generated sea. These larger waves may impact the rate of spume generation, the size of droplets produced, and their vertical transport and distribution above breaking waves. This appears to be the case because the differences between water types across the various studies are much smaller than simply the aggregate difference in observed spume concentration between these two studies. Given the limitations of both experiments, a more robust intercomparison was not possible. Unsatisfactorily, the primary

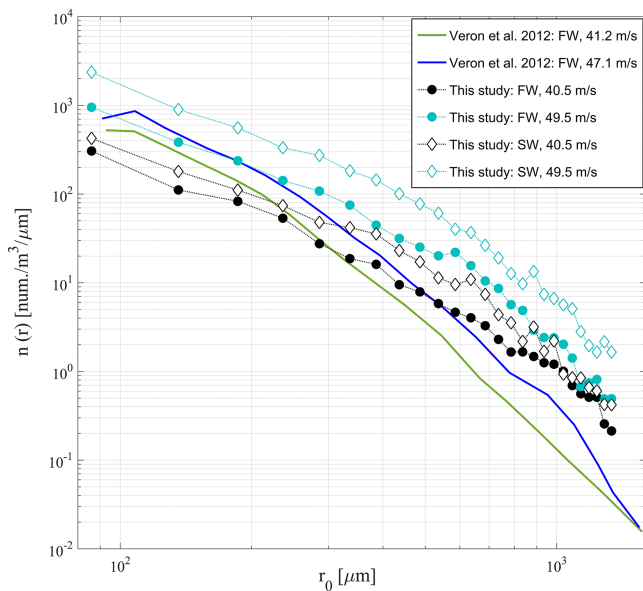


**Figure 9.** A comparison of the number concentration spectra for freshwater (FW) and seawater (SW) at two wind speeds ( $U_{10} = 40.5$  and  $49.5$  m/s) from this study and the observations from Veron et al. (2012) at  $U_{10} = 41.2$  and  $47.1$  m/s for FW. The spectra from this study are vertical averages of the lowest six bins of the profile.

setup, but, relative to the general uncertainty with spume concentrations across this radius subrange, the radius-dependent spectra between these two experiments agree fairly well. Furthermore, this agreement, in terms of spray concentration for a given wind speed, tends to become better when comparing the FW spectra from our study to the results from Veron et al. (2012), especially for a wind speed above 45 m/s.

#### 4.3. Differences Between FW and SW

The results of this experiment demonstrated that there are significant differences in the radius- and wind speed-dependent spume generation processes between FW and SW. A limitation of this experiment was that the physiochemical mechanism(s) controlling these observations could not be directly quantified; however, it is possible to speculate on the potential factors controlling the observed spray distributions. Further study will be needed to corroborate these hypotheses and fully establish the mechanism(s) responsible for the differences captured by these experiments. This will ultimately facilitate the more physically realistic modeling of spume generation and spray-mediated processes at the air-sea interface.

There are two major components to discuss: (1) the greater rate of droplet generation in SW versus FW and (2) the relatively constrained vertical transport of entrained droplets in the air above SW relative to above FW. Given the controlled environment of the laboratory, it is plausible that physiochemical difference(s) between FW and SW play a significant role in the spray generation process. From a purely chemical perspective, the distinct impact of dissolved ions (e.g.,  $\text{Na}^+$ ,  $\text{Cl}^-$ ,  $\text{SO}_4^{2-}$ ,  $\text{Mg}^{2+}$ , and others in seawater) in water is to disrupt the intermolecular bonding between water molecules (i.e., cohesion). These nonchemical bonds are known as van der Waals forces, and they are strongest in pure water and progressively weaken with the addition of dissolved material—at the same fluid temperature. This reduction in cohesion from FW to SW could facilitate the mechanical tearing of spume droplets from the water surface by the wind or the ejection of spume from the breaking wave crest.

The more commonly discussed water property (in air-sea interaction research), surface tension, is directly related to water cohesion and the molecular Van Der Waals forces (Auluck & Rai, 1944) but is limited to the molecular layer at the surface of the water. Surface tension is critical to capillary wave development and damping in the presence of surfactants (Jarvis et al., 1967). While surface tension, which can inhibit film and jet droplet generation, is larger in SW than FW, given the strongly forced and highly turbulent regime

conclusion one can draw from comparing our work to Fairall et al. (2009) is that significantly more work is needed to fill gaps in our understanding of the varying role of salinity and different sea states has on spume generation.

We also compared our results to the experiments summarized in Veron et al., 2012; Figure 9). These previous experiments represent a more equitable comparison (as opposed to Fairall et al.'s work) because both the laboratory setup and observational techniques were very similar. The major difference was that Veron et al. only used FW—interestingly because they relied on the assumption that salinity does *not* impact spume production. For comparison, the lowest six vertical cells of the concentration profiles from our study were averaged and compared to the spectra from Veron et al. (2012; the work presented vertically integrated concentration spectra). In this case, the effective scaled height of the present and previous work was  $z/H_s \sim 2.5$  and 1, respectively. For smaller drops (up to 250–300  $\mu\text{m}$ ), the magnitudes of  $n(r)$  observed in Veron et al. (2012) were very similar to  $n(r)_{\text{FW}}$  from our study. For both of these studies, the radius dependences of the  $n(r)$  were remarkably similar and exhibited dependences around  $r^{-1.96}$  and  $r^{-1.8}$ . However, from medium to larger radii drops ( $>300$   $\mu\text{m}$ ), the spectra from this study diverge from Veron et al. (2012).

Our observations showed a slightly shallower radius falloff and thus a higher concentration of large particles approaching the 1-mm radius.

Some of these differences may be attributed to variable experimental

under investigation, it seems unlikely that the surface tension, and/or the presence of surfactants (more readily generated in SW), is primarily responsible for the observations presented here. On the other hand, cohesion is an internal property of the fluid and not altered by disruption of the fluid's surface. Although the physiochemical differences of FW and SW are small in absolute terms, these are distinct liquids and, while the mechanical processes of wave breaking and wind forcing are the primary drivers for spume generation, regardless of water type, the observations reported here suggest that the secondary effect of the liquid's properties could play a role in the generation process.

Another plausible factor contributing to (1) may be that the increased concentration of subsurface bubbles in SW, versus FW, may disrupt the surface at the crest and wind-ward side of the wave face, thereby facilitating spume generation. It has been well established that bubbles are more numerous (and smaller) in SW as compared to FW (Haines & Johnson, 1995), due to the presence of dissolved ions reducing the surface elasticity and limiting large bubble growth through a shattering mechanism (Christenson & Yaminsky, 1995). While spume is not generated by individual bubble bursting (Veron 2015), the combined action of many bubbles breaking at the surface and/or rising to the very near surface layer could facilitate the generation of spume via the shearing forcing of the tangential wind stress of water surface. This effect, if present, would be expected to be larger in SW due to the much larger bubble population as compared to FW.

Once entrained in the air, the differences in vertical distribution between FW and SW might be explained by the turbulent air flow suppression/mediation due to the development of a significantly more densely populated spray layer in SW versus FW. The higher concentration of SW particles could disrupt the turbulent air flow, thus inhibiting their own vertical transport as compared to FW particles forced by the same background wind speed. A factor that may contribute to this is the larger quantities of small droplets,  $r_0 < 80 \mu\text{m}$ , generated in SW than FW due to our hypothesized bubble generation mechanisms. While these droplets were not resolved in the study, they were present in the control volume and contributed to the overall density of the entrained spray layer. Theoretically, it has been hypothesized that the spray layer acts as an intermediate "third fluid" layer between the conventionally binary air-water interfaces (Lighthill, 1999). Furthermore, Lykossov (2001) argues that spray would disrupt the logarithmic wind profile, which fundamentally depends on a known relationship between the free stream wind velocity and the near-surface turbulence generation. Barenblatt et al. (2005) provided a mathematical model to corroborate Lighthill's theory and demonstrated, in a highly idealized scenario, that the presence of spray inhibits turbulence intensity and drastically reduces the aerodynamic drag coefficient of the ocean surface. Recently, high-resolution model simulations have shown that the turbulent energy differs significantly for the spray-laden versus spray-free air flow over waves (Pan et al., 2019; Richter & Sullivan, 2013; Tang et al., 2017).

Another possible contributing factor to the finding that droplets from seawater are not as uniformly distributed vertically as freshwater is the varying density between the two water types. Assuming that all other variables (droplet size, wind speed, etc.) are equal, the droplet deposition velocity  $V_d$  is directly proportional to the difference between the densities of the droplet and the air mass. The conventional form of  $V_d$  (Fairall et al., 1994) is a simple parameterization that is fundamentally based on the terminal velocity of a quasi-spherical drop of water (Pruppacher & Klett 1997, Figures 10–123 and equations 10–198 and 10–199). This approach is flawed, but without a more suitable alternative it remains a standard approach to estimating the spray flux into the atmosphere (e.g., Ortiz-Suslow et al., 2016). The ratio of the densities between SW and FW is  $\sim 1.028$  or  $\sim 2.8\%$ . This translates to an equivalent difference in  $V_d$ , with all other variables held constant. For a droplet with  $r_0 = 100 \mu\text{m}$ , this creates a relative deposition velocity of  $-0.028 \text{ m/s}$  between FW and SW. Assuming two identical droplets (one FW and one SW) are ejected from the same wave crest at the same trajectory and entrained into the same air flow, with a residence time  $O(1)$  second (approximation based on Andreas et al., 2010, Figure 3) they become vertically separated by a maximum of  $\sim 30 \text{ mm}$ , or  $\sim 1 z/H_s$  at our lowest wind speed tested. Given our entire profile ranged from  $2\text{--}6 z/H_s$ , this represents a significant spatial separation solely attributed to density differences. We would note that this disparity may be more emphasized in a laboratory-scale environment and it is unknown if this has a substantial impact, for spume drops,  $80 < r_0 < 1,200 \mu\text{m}$ , over geophysical water bodies.

There is an important limitation in this study that must be noted. During the individual trials conducted as part of this experiment, the water temperature in the tank was not recorded. Prior to every trial and/or after changing water masses in the tank, the volume was given a period of time (at least one full day) to acclimate

to the climate-controlled laboratory. Furthermore, because of the trials were run in a closed-circuit mode, that is, no outside airflow, the air-sea temperature regime would be approximately thermodynamically neutral. Given these conditions, we do not feel that there would be substantial differences in temperature across the various trials. Nonetheless, this remains a caveat to the work presented here. Unfortunately, between the conclusion of these experiments and this analysis, ASIST was moved to a new facility and setup in such a way as to preclude simply redoing the experiments.

## 5. Conclusions

Here we present the results of the first quantitative comparison between fresh and seawater spume generation in hurricane-force winds. The aim of this study was to directly test whether or not water type has an impact on spume generation via wave breaking. Using a nonintrusive optical technique in the laboratory, spume droplets were observed in the radius range of 80–1,400 μm, and the dependence of droplet concentration was investigated in terms of wind speed, particle size, and height above the waves for both water types. We have reported three primary results: (1) seawater spume was observed in significantly higher quantities as compared to freshwater, (2) the vertical distribution of seawater spume was concentrated closer to the water surface as compared to freshwater, and (3) size-dependent distributions respond significantly differently in sea and freshwater to increasing wind speed.

Collectively, the findings of this experiment point to substantial differences in the spume concentration between these two water types, suggesting that the physiochemical properties of the medium may be of importance in this process. The results of this experiment hold implications for modeling spray-mediated fluxes over the real ocean, in addition to large fresh water bodies. Additional work is needed incorporating mixed water mass having a range of salinity focusing on better understanding the mechanism controlling these differences, as well as incorporating other processes known to impact spume generation, such as non-wind-driven waves.

## Acknowledgments

This work was funded by NSF through Grant 0933943. Additional support was provided through ONR phase-resolved wave program under Grant N000141410644. We appreciate the efforts of Mike Rebozo and Dr. Neil Williams for the help with the data collection. We would also like to especially thank Dr. Andrew Margolin for his helpful discussions in conceptualizing the findings of this study. We must acknowledge the rigorous and careful review of an anonymous reviewer, whose prodigious efforts unquestionably improved the quality and communicability of this study. Data are archived at the University of Miami repository under the name Spray Concentration Measurements from ASIST for Freshwater and Seawater.

## References

- Andreas, E. L. (1992). Sea spray and the turbulent air-sea heat fluxes. *Journal of Geophysical Research*, 97(C7), 11,429–11,441. <https://doi.org/10.1029/92JC00876>
- Andreas, E. L. (2004). Spray stress revisited. *Journal of Physical Oceanography*, 34(6), 1429–1440. [https://doi.org/10.1175/1520-0485\(2004\)034<1429:SSR>2.0.CO;2](https://doi.org/10.1175/1520-0485(2004)034<1429:SSR>2.0.CO;2)
- Andreas, E. L. (2011). Fallacies of the enthalpy transfer coefficient over the ocean in high winds. *Journal of the Atmospheric Sciences*, 68(7), 1435–1445. <https://doi.org/10.1175/2011AS3714.1>
- Andreas, E. L., & Emanuel, K. A. (2001). Effects of sea spray on tropical cyclone intensity. *Journal of the Atmospheric Sciences*, 58(24), 3741–3751. [https://doi.org/10.1175/1520-0469\(2001\)058<3741:EOSSOT>2.0.CO;2](https://doi.org/10.1175/1520-0469(2001)058<3741:EOSSOT>2.0.CO;2)
- Andreas, E. L., Jones, K. F., & Fairall, C. W. (2010). Production velocity of sea spray droplets. *Journal of Geophysical Research*, 115, C12065. <https://doi.org/10.1029/2010JC006458>
- Andreas, E. L., Mahrt, L., & Vickers, D. (2015). An improved bulk air-sea surface flux algorithm, including spray-mediated transfer. *Quarterly Journal of the Royal Meteorological Society*, 141(687), 642–654. <https://doi.org/10.1002/qj.2424>
- Auluck, F. C., & Rai, R. N. (1944). Surface tension and van der Waals' equation. *The Journal of Chemical Physics*, 12(7), 321–322. <https://doi.org/10.1063/1.1723948>
- Balaguru, K., Chang, P., Saravanan, R., Leung, L. R., Xu, Z., Li, M., & Hsieh, J. S. (2012). Ocean barrier layers' effect on tropical cyclone intensification. *Proceedings of the National Academy of Sciences*, 109(36), 14,343–14,347. <https://doi.org/10.1073/pnas.1201364109>
- Bao, J. W., Fairall, C. W., Michelson, S. A., & Bianco, L. (2011). Parameterizations of sea-spray impact on the air-sea momentum and heat fluxes. *Monthly Weather Review*, 139(12), 3781–3797. <https://doi.org/10.1175/MWR-D-11-00007.1>
- Barenblatt, G. I., Chorin, A. J., & Prostokishin, V. M. (2005). A note concerning the Lighthill "sandwich model" of tropical cyclones. *Proceedings of the National Academy of Sciences*, 102(32), 11,148–11,150. <https://doi.org/10.1073/pnas.0505209102>
- Bianco, L., Bao, J. W., Fairall, C. W., & Michelson, S. A. (2011). Impact of sea-spray on the atmospheric surface layer. *Boundary-Layer Meteorology*, 140(3), 361–381. <https://doi.org/10.1007/s10546-011-9617-1>
- Blanchard, D. C., & Syzdek, L. D. (1988). Film drop production as a function of bubble size. *Journal of Geophysical Research*, 93(C4), 3649–3654. <https://doi.org/10.1029/JC093iC04p03649>
- Christenson, H. K., & Yaminsky, V. V. (1995). Solute effects on bubble coalescence. *The Journal of Physical Chemistry*, 99(25), 10,420–10,420. <https://doi.org/10.1021/j100025a052>
- Donelan, M. A., Haus, B. K., Reul, N., Plant, W. J., Stiassnie, M., Gruber, H. C., & Saltzman, E. S. (2004). On the limiting aerodynamic roughness of the ocean in very strong winds. *Geophysical Research Letters*, 31, L18306. <https://doi.org/10.1029/2004GL019460>
- Fairall, C. W., Banner, M. L., Peirson, W. L., Asher, W., & Morison, R. P. (2009). Investigation of the physical scaling of sea spray spume droplet production. *Journal of Geophysical Research*, 114, C10001. <https://doi.org/10.1029/2008JC004918>
- Fairall, C. W., Kepert, J. D., & Holland, G. J. (1994). The effect of sea spray on surface energy transports over the ocean. *Global Atmosphere and Ocean System*, 2, 121–142.
- Haines, M. A., & Johnson, B. D. (1995). Injected bubble populations in seawater and freshwater measured by a photographic method. *Journal of Geophysical Research*, 100(C4), 7057–7068. <https://doi.org/10.1029/94JC03226>

- Haus, B. K., Jeong, D., Donelan, M. A., Zhang, J. A., & Savelyev, I. (2010). Relative rates of sea-air heat transfer and frictional drag in very high winds. *Geophysical Research Letters*, 37, L07802. <https://doi.org/10.1029/2009GL042206>
- Jarvis, N. L., Garrett, W. D., Scheiman, M. A., & Timmons, C. O. (1967). Surface chemical characterization of surface-active material in seawater. *Limnology and Oceanography*, 12(1), 88–96. <https://doi.org/10.4319/lo.1967.12.1.00088>
- Jeong, D., Haus, B. K., & Donelan, M. A. (2012). Enthalpy transfer across the air–water interface in high winds including spray. *Journal of the Atmospheric Sciences*, 69(9), 2733–2748. <https://doi.org/10.1175/JAS-D-11-0260.1>
- Lighthill, J. (1999). Ocean spray and the thermodynamics of tropical cyclones. *Journal of Engineering Mathematics*, 35(1/2), 11–42. <https://doi.org/10.1023/A:1004383430896>
- Lykossov, V. (2001). Atmospheric and oceanic boundary layer physics. In I. Jones, & Y. Toba (Eds.), *Wind Stress Over the Ocean*, (pp. 54–81). New York, NY: Cambridge University Press.
- MacIntyre, F. (1972). Flow patterns in breaking bubbles. *Journal of Geophysical Research*, 77(27), 5211–5228. <https://doi.org/10.1029/JC077i027p05211>
- Monahan, E., Niocaill, G., & Koepke, P. (1986). Oceanographic Sciences Library, Vol. 2.
- Monahan, E. C. (1967). A study of the onset of white capping with increased surface wind speeds; and a report on a preliminary drift-bottle study of the surface currents of Lake Superior (no. tr-1). Northern Michigan University Marquette Dept of physics.
- Monahan, E. C. (1972). Oceanic whitecaps. *Journal of Physical Oceanography*, 1, 139–144.
- Monahan, E. C., Fairall, C. W., Davidson, K. L., & Jones-Boyle, P. (1983). Observed inter-relations between 10 m winds, ocean whitecaps and marine aerosols. *Quarterly Journal of the Royal Meteorological Society*, 109(460), 379–392. <https://doi.org/10.1002/qj.49710946010>
- Monahan, E. C., Stanić, A., & Vlahos, P. (2017). Spume drops: Their potential role in air-sea gas exchange. *Journal of Geophysical Research: Oceans*, 122, 9500–9517. <https://doi.org/10.1002/2017JC013293>
- Monahan, E. C., & Zietlow, C. R. (1969). Laboratory comparisons of fresh-water and salt-water whitecaps. *Journal of Geophysical Research*, 74(28), 6961–6966. <https://doi.org/10.1029/JC074i028p06961>
- Mueller, J. A., & Veron, F. (2009). A sea state-dependent spume generation function. *Journal of Physical Oceanography*, 39(9), 2363–2372.
- Ortiz-Suslow, D. G., Haus, B. K., Mehta, S., & Laxague, N. J. (2016). Sea spray generation in very high winds. *Journal of the Atmospheric Sciences*, 73(10), 3975–3995. <https://doi.org/10.1175/JAS-D-15-0249.1>
- Pan, M., Liu, C., Li, Q., Tang, S., Shen, L., & Dong, Y. (2019). Impact of spray droplets on momentum and heat transport in a turbulent marine atmospheric boundary layer. *Theoretical and Applied Mechanics Letters*, 9(2), 71–78. <https://doi.org/10.1016/j.taml.2019.02.002>
- Potter, H., Gruber, H. C., Williams, N. J., Collins, C. O. III, Ramos, R. J., & Drennan, W. M. (2015). In situ measurements of momentum fluxes in typhoons. *Journal of the Atmospheric Sciences*, 72(1), 104–118. <https://doi.org/10.1175/JAS-D-14-0025.1>
- Powell, M. D., Vickery, P. J., & Reinhold, T. A. (2003). Reduced drag coefficient for high wind speeds in tropical cyclones. *Nature*, 422(6929), 279–283. <https://doi.org/10.1038/nature01481>
- Pruppacher, H. R., & Klett, J. D. (1997). Microphysics of clouds and precipitation: Reprinted 1980. Springer Science & Business Media. (Fig. 10-23, eqns. 10-138-139)
- Resch, E., & Afeti, G. (1991). Film drop distributions from bubbles bursting in seawater. *Journal of Geophysical Research*, 96(C6), 10,681–10,688. <https://doi.org/10.1029/91JC00433>
- Richter, D. H., & Sullivan, P. P. (2013). Momentum transfer in a turbulent, particle-laden Couette flow. *Physics of Fluids*, 25(5), 053304. <https://doi.org/10.1063/1.4804391>
- Rudzin, J. E., Shay, L. K., & Jaimes de la Cruz, B. (2019). The impact of the Amazon-Orinoco River plume on enthalpy flux and air-sea interaction within Caribbean Sea tropical cyclones. *Monthly Weather Review*, 147(3), 931–950. <https://doi.org/10.1175/MWR-D-18-0295.1>
- Slaurenwhite, D. E., & Johnson, B. D. (1999). Bubble shattering: Differences in bubble formation in fresh water and seawater. *Journal of Geophysical Research*, 104(C2), 3265–3275. <https://doi.org/10.1029/1998JC000064>
- Soloviev, A. V., Lukas, R., Donelan, M. A., Haus, B. K., & Ginis, I. (2014). The air-sea interface and surface stress under tropical cyclones. *Scientific Reports*, 4, 5306.
- Soloviev, A. V., Lukas, R., Donelan, M. A., Haus, B. K., & Ginis, I. (2017). Is the state of the air-sea interface a factor in rapid intensification and rapid decline of tropical cyclones? *Journal of Geophysical Research: Oceans*, 122, 10,174–10,183. <https://doi.org/10.1002/2017JC013435>
- Spiel, D. E. (1997). More on the births of jet drops from bubbles bursting on seawater surfaces. *Journal of Geophysical Research*, 102(C3), 5815–5821. <https://doi.org/10.1029/96JC03582>
- Spiel, D. E. (1998). On the births of film drops from bubbles bursting on seawater surfaces. *Journal of Geophysical Research*, 103(C11), 24,907–24,918. <https://doi.org/10.1029/98JC02233>
- Takagaki, N., Komori, S., Suzuki, N., Iwano, K., Kuramoto, T., Shimada, S., & Takahashi, K. (2012). Strong correlation between the drag coefficient and the shape of the wind sea spectrum over a broad range of wind speeds. *Geophysical Research Letters*, 39, L23604. <https://doi.org/10.1029/2012GL053988>
- Tang, S., Yang, Z., Liu, C., Dong, Y. H., & Shen, L. (2017). Numerical study on the generation and transport of spume droplets in wind over breaking waves. *Atmosphere*, 8(12), 248. <https://doi.org/10.3390/atmos8120248>
- Troitskaya, Y., Kandaurov, A., Ermakova, O., Kozlov, D., Sergeev, D., & Zilitinkevich, S. (2018). The “bag breakup” spume droplet generation mechanism at high winds. Part I: Spray generation function. *Journal of Physical Oceanography*, 48(9), 2167–2188. <https://doi.org/10.1175/JPO-D-17-0104.1>
- Veron, F. (2015). Ocean spray. *Annual Review of Fluid Mechanics*, 47, 507–538.
- Veron, F., Hopkins, C., Harrison, E. L., & Mueller, J. A. (2012). Sea spray spume droplet production in high wind speeds. *Geophysical Research Letters*, 39, L16602. <https://doi.org/10.1029/2012GL052603>